# Electropolymerized Polyaniline Stabilized Tungsten Oxide Nanocomposite Films: Electrochromic Behavior and Electrochemical Energy Storage

Huige Wei,[†,‡] Xingru Yan,[†,‡] Shijie Wu,[§] Zhiping Luo,[∥] Suying Wei,*[,‡] and Zhanhu Guo*[,†]

[†]Integrated Composites Laboratory (ICL), Dan F. Smith Department of Chemical Engineering, and [‡]Department of Chemistry and Biochemistry, Lamar University, Beaumont, Texas 77710, United States

[§]Agilent Technologies, Inc., Chandler, Arizona 85226, United States

[∥]Department of Chemistry and Physics and Southeastern North Carolina Regional Microanalytical and Imaging Consortium, Fayetteville State University, Fayetteville, North Carolina 28301, United States

**S** *Supporting Information*

**ABSTRACT:** Polyaniline (PANI)/tungsten oxide ($WO_3$) nanocomposite films were fabricated by electropolymerization of aniline monomers onto $WO_3$ coated indium tin oxide (ITO) glass slides, which were prepared by spin coating technique and followed by annealing at 500 °C for 2 h. The morphology and crystalline structure of the composite films were studied using Fourier transform infrared (FT-IR) spectroscopy, atomic force microscopy (AFM), X-ray diffraction (XRD), and transmission electron microscopy (TEM). The results confirm chemical interactions between the polymer matrix and the $WO_3$ particles and reveal a well crystallized PANI/$WO_3$ nanocomposite structure. The optical properties and electrochemical capacitive behaviors of the composite films for electrochromic (EC) and energy storage devices applications were investigated using spectroelectrochemistry (SEC), cyclic voltammetry (CV) and galvanostatic charge−discharge measurements. The composite films show dual electrochromism at both positive and negative potentials arising from PANI and $WO_3$, respectively. A coloration efficiency of 98.4 $cm^2$ $C^{-1}$ was obtained for the composite film, which was much higher than that of $WO_3$ (36.3 $cm^2$ $C^{-1}$) and PANI (50.0 $cm^2$ $C^{-1}$) thin film. An areal capacitance of 0.025 F $cm^{-2}$ that is comparable to that of pure PANI (0.075 F $cm^{-2}$) is derived from CV at a scan rate of 5 mV/s with a broader working potential window of 1.3 V. The cyclic stability studies reveal that the composite films exhibit much more enhanced durability and retain significant charge storage or discharge capacity after 1000 charge−discharge cycles. However, pure PANI loses most of the charge storage or discharge capacity after 350 cycles. The chemical bonding between PANI matrix and $WO_3$ particles is believed to play an important role in enhancing the stability of the nanocomposite film.
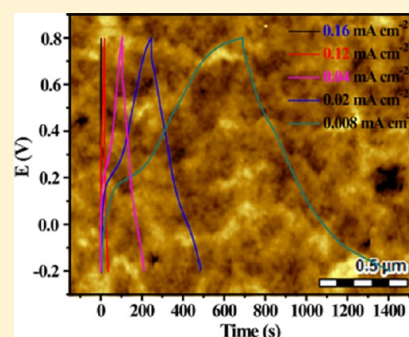
## 1. INTRODUCTION

A strategy of combining conjugated polymers (CPs) and inorganic materials for applications in various domains of electronics, for example, as active layers in light emitting diodes (LEDs), photodiodes, and photovoltaic cells, has been deployed and widely studied in recent years.[1−5] It turns out that these new hybrid materials may lead to polymer nanocomposites (PNCs) with properties unmatched by conventional counterparts. PNCs based on CPs including polythiophene,[6,7] polypyrrole (PPy),[8,9] poly(DNTD),[10−12] polyaniline (PANI),[13,14] and their derivatives have attracted intense interest. Particularly, PANI has received special attention because of its intriguing properties such as facile polymerization in aqueous media[15−18] or nonaqueous media,[19] versatile redox behavior, good stability in air, low cost, high conductivity, and high pseudocapacitance.[20,21] The promising potential applications of PANI-based composites, for example, graphene/PANI, for supercapacitors,[22−24] energy, and environmental remediations[25−27] have been recently explored and investigated.

With regard to inorganic materials for the fabrication of PNCs, semiconductive metal oxides are of intense interest due to their possessing complementary properties.[28] For example, $TiO_2$,[29,30] $ZnO$,[31] $MoO_3$,[32] and $Fe_3O_4$[33] were incorporated in CPs to prepare hybrid materials for organic electronics, photocatalysts, and sensor applications. As an n-type semiconductor with a band gap of 2.7 eV, $WO_3$ is mostly investigated among the many inorganic materials owing to its many advantages including genuine color switching, good chemical stability, and strong adherence to substrate.[34−38] $WO_3$ has been successfully utilized in photoelectrocatalytic processes, electrochromic devices, dye-sensitized solar cells, gas sensors, and electrocatalysis. $WO_3$ of different structures (nanowire,[39] nanorod,[40] and mesopore[41,42]) has been prepared by methods including a hydrothermal process,[39,40] sol−gel derived spin or dip coating methods,[43,44]
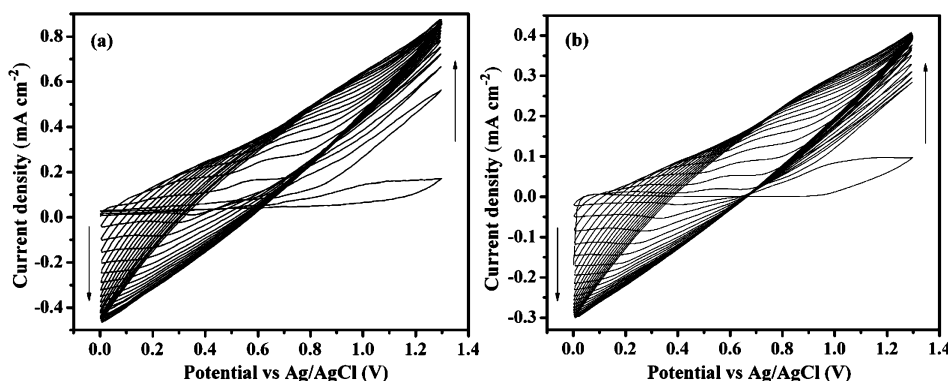
**Figure 1.** Electropolymerization synthesis of PANI onto (a) bare and (b) $WO_3$ coated ITO glass slides at a scan rate of 50 mV/s in 0.5 M $H_2SO_4$ aqueous solution containing 0.1 M aniline.

and sputtering.[45,46] The sol–gel method has been preferred for preparing amorphous electrochromic $WO_3$ films, which allow for obtaining homogeneous finely grained ceramics and offer the control of chemical purity and crystallinity.[47] The sol–gel obtained from the reaction between hydrochloric acid and tungsten ethoxide proves to be a suitable way to prepare $WO_3$ films free of foreign ions, thus avoiding the impurity of sol–gel when the alkaline sodium tungstate and hydrochloric acid are used as the starting materials.[48]

$WO_3$ is a typical cathodic coloration material and PANI is an anodic coloration material.[20,49] Interestingly, these two materials have similar ion exchange properties. For example, both can exchange with $H^{+}$[21] or $Li^{+}$[50] in solution. Also, both are electron and proton conductors. However, single color changes (between blue and transparent), slow switching speed of $WO_3$, and relatively low electrochemical stability of PANI impose limitations for their applications.[51,52] A recent study has shown that the PANI/$WO_3$ hybrids prepared by oxidation polymerization or electropolymerization of PANI onto $WO_3$ foils show both p- and n-type photoelectrochemical activity.[53] The separation of electroactivity within the applied potential window without losing any electroactivity due to the presence of the other component is advantageous for the utilization of such composites for electrochromic applications. However, a comprehensive study of electrochromic behaviors and electrochemical energy storage of these nanocomposite films, to the best of our knowledge, has not been reported yet.

In this work, the PANI/$WO_3$ nanocomposite films of complementary properties from both materials are prepared by a facile method, in which aniline monomers in sulfuric acid solutions were electrodeposited onto sol–gel method obtained $WO_3$ films. The morphology and structure of the composite films were studied using Fourier transform infrared (FT-IR) spectroscopy, atomic force microscopy (AFM), X-ray diffraction (XRD), and transmission electron microscopy (TEM). The optical properties and capacitive behaviors of these composite films for electrochromic (EC) and energy storage device applications were investigated using spectroelectrochemistry (SEC), cyclic voltammetry (CV), and galvanostatic charge–discharge measurements.

## 2. EXPERIMENTAL SECTION

**2.1. Materials.** Tungsten(VI) ethoxide was purchased from Alfa-Aesar, and aniline was purchased from Sigma Aldrich. The microscope glass slides and indium tin oxide (ITO) coated glass slides were purchased from Fisher and NanoSci Inc., respectively.

ITO coated glass slides were sonicated in ethanol for 10 min, then immersed in an aqueous solution containing 1 mL of 28.86 wt % ammonium hydroxide, 1 mL of 30.0 wt % hydrogen peroxide (both from Fisher), and 5 mL of deionized water for 10 min, and sonicated in deionized water for 10 min before usage.

**2.2. Preparation of PANI/$WO_3$ Composite Films.** The $WO_3$ sol–gel film was prepared according to ref 54. Briefly, tungsten ethoxide (0.5 g) was dissolved in 125 mL of ethanol. The solution was stirred at 75 °C for 3 h, and then 0.5 mL of distilled water containing $3.5 \times 10^{-4}$ g of HCl was added for hydrolysis with vigorous stirring at room temperature. Ethanol was allowed to gently evaporate until 50 mL of sol solution remained. The sol was spun onto ITO glass slide at 2000 rpm for 20 s, and then the film was annealed at 500 °C in air at a heating rate of 2 °C $min^{-1}$ for 2 h and cooled naturally in air.

Electropolymerization of aniline onto $WO_3$ film was performed on an electrochemical working station, VersaSTAT 4 potentiostat (Princeton Applied Research). A typical electrochemical cell consisting of a reference electrode, a working electrode, and a counter electrode was employed. An Ag/AgCl electrode saturated with KCl served as the reference electrode, and a platinum (Pt) wire served as the counter electrode. The $WO_3$ coated ITO glass slide with an effective area of 5 $cm^2$ served as the working electrode. A long path length homemade spectroelectrochemical cell with Teflon cell body with front and rear windows clapped with two steel plates was used when the ITO glass slide was used as the working electrode for optical characterizations. A typical electrochemical polymerization was performed for 30 cycles scanned back and forth from 0 to 1.3 V vs Ag/AgCl at a scan rate of 50 mV/s in 0.5 M $H_2SO_4$ aqueous electrolyte containing 0.1 M aniline.

**2.3. Characterization.** The morphology of the thin films grown on the ITO glass slides was characterized by atomic force microscopy (AFM; Agilent 5600 system with multipurpose 90 $\mu$m scanner) and a scanning electron microscope (SEM; FEI Quanta 200F). Imaging of AFM was done in acoustic ac mode (AAC) using a silicon tip with a force constant of 2.8 N/m and a resonance frequency of 70 kHz.

An FT-IR spectrometer coupled with an ATR accessory (Bruker Inc. Vector 22) was used to characterize the surface functionality of the thin films grown on the ITO glass slides in the range 1700–700 $cm^{-1}$ at a resolution of 4 $cm^{-1}$.

X-ray diffraction (XRD) analysis was carried out with a Bruker AXS D8 Discover diffractometer with GADDS (general area detector diffraction system) operating with a Cu $K\alpha$ radiation

source filtered with a graphite monochromator ($\lambda = 1.5406$ Å). Data were collected in the range 2–80°.

The crystalline structure of the thin films was further characterized by a high resolution transmission electron microscope (HRTEM; FEI Tecnai G2 F20) with a field emission gun, operated at an accelerating voltage of 200 kV. The TEM samples were prepared by drying a drop of ethanol suspension on carbon-coated copper TEM grids.

The electrochemical properties of the $WO_3$ sol–gel films and the $PANI/WO_3$ hybrid films were investigated by CV scanned from −0.5 to 0.8 V vs Ag/AgCl at a scan rate of 10 mV/s in 0.5 M $H_2SO_4$ aqueous solution. The spectroelectrochemistry measurements were performed on a Jasco V-670 spectrophotometer coupled with the potentiostat for applying electrochemical potentials. In situ chronocoulometry (CC) was conducted under a square-wave voltage of 0.8 and −0.2 V with a pulse width of 20 s.

The electrochemical energy storing behaviors of the films were studied by CV at a series of scan rates and galvanostatic charge–discharge measurements in 0.5 M $H_2SO_4$ aqueous solution. The endurance of the films was also assessed using charge–discharge measurements switched between 0.8 and −0.2 V holding for 10 s, respectively, for 1000 cycles.

## 3. RESULTS AND DISCUSSION

**3.1. Synthesis of PANI/WO$_3$ Hybrid Films.** Parts a and b of Figure 1 show the cyclic voltammograms (CVs) obtained during the potentiodynamic electropolymerization of PANI grown onto bare and $WO_3$ coated ITO glass slides, respectively. Pure PANI films or $PANI/WO_3$ nanocomposite films were prepared by sweeping the potential between 0 and +1.3 V at a scan rate of 50 mV $s^{-1}$ in aqueous solution containing 0.1 M aniline and 0.5 M $H_2SO_4$. These two films exhibit similar CV patterns except that lower anodic current peaks are observed for the $PANI/WO_3$ composite film growth, which is attributed to the increased resistance of $WO_3$ film on the ITO. For both films, an anodic peak starting around +0.9 V corresponds to the oxidation of aniline monomers, which initiated the electropolymerization of PANI.[55] In the following scans, the current increased with increasing cycles, reflecting the growth of pure polymer and nanocomposite thin films. The anodic and cathodic peaks show the oxidation and reduction of the PANI film. Correspondingly, color switching from green (emeraldine salt, ES) to blue (pernigraniline salt, PS) can be observed.

These voltammograms on ITO were different from the CVs usually obtained by electropolymerization of PANI on platinum electrodes that commonly exhibit well-defined redox peaks corresponding to a series of redox transitions: oxidation of the fully reduced insulating form (leucoemerladine) to its radical cation (polaron, emeraldine), followed by the oxidation of degradation products and/or intermediate species, and finally the transition from the delocalized polaronic state to a localized bipolaron or quinoid form (pernigraniline).[55,56] The reason for different voltammogram behaviors between the films on indium tin oxide and Pt electrodes might lie in the conductivity difference of the substrates that renders the electropolymerization easier on Pt than on ITO substrates.[57–59]

**3.2. Morphology and Composition Analysis.** *3.2.1. FT-IR Analysis.* Curves a, b, and c in Figure 2 show the FT-IR spectra of the $WO_3$ film, PANI film, and $PANI/WO_3$ composite film in the region 1700–700 $cm^{-1}$, respectively. In Figure 2a, the peak at 920 $cm^{-1}$ is attributed to the asymmetric stretching mode of terminal W═O,[38] and the peaks at 874, 764, and 830 $cm^{-1}$ are
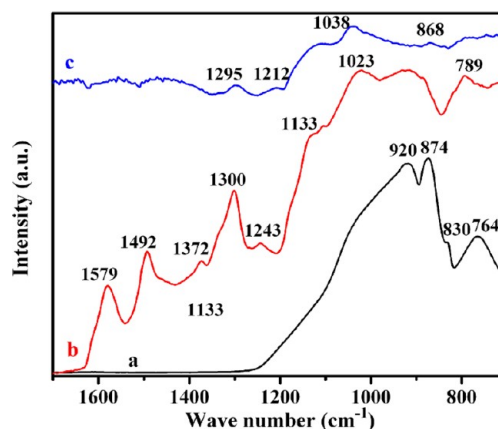


**Figure 2.** FT-TR spectra of (a) $WO_3$, (b) PANI, and (c) $PANI/WO_3$ nanocomposite films.

ascribed to the stretching mode of W−O−W in $WO_3$.[44] For the PANI thin film onto ITO using multiple CV methods, Figure 2b, the peaks at 1579 and 1492 $cm^{-1}$ correspond to the characteristic C−C stretching modes of the quinoid and benzenoid rings, respectively.[60] The peaks at 1133 and 787 $cm^{-1}$ are assigned to the in-plane and out-of-plane bending of C−H.[61,62] The peaks at 1300 and 1246 $cm^{-1}$ are attributed to the C−N and C═N stretching modes.[63,64] When PANI is electropolymerized onto $WO_3$ thin film, the peaks at 1300 and 1243 $cm^{-1}$ corresponding to C−N and C═N stretching modes of the polymer matrix are shifted to lower wavenumbers at 1295 and 1212 $cm^{-1}$, respectively, and a peak at 874 $cm^{-1}$ attributed to the W−O−W stretching mode can also be observed shifted to 868 $cm^{-1}$. These shifts indicate the chemical bonding between the PANI matrix and $WO_3$ particles. The nitrogen atoms in PANI are inferred to form coordinated compounds with the exposed tungsten atoms on the surface of $WO_3$, just as in the case of $PANI/TiO_2$ hybrids[60,65] (see Scheme 1). The strong ionic (or covalent) bonds between the nitrogen atom and the tungsten atom might cause the observed peak shifts.

*3.2.2. Crystalline Structure from XRD and HRTEM Analysis.* Figure 3 shows the XRD patterns of the films. The $WO_3$ film annealed at 500 °C reveals a crystalline structure, and its XRD patterns are quite similar to those reported.[66] In Figure 3b, the two broad peaks at $2\theta = 22.8$ and 26.9° correspond to the (100) and (110) crystal planes of the partially crystalline PANI.[64,67] The lower peak intensity of the PANI film electropolymerized on ITO glass slide compared to that of PANI particles prepared by chemical synthesis might be due to the different preparation methods[68] and the thin thickness of the film. Interestingly, the peaks for the composite film become much sharper, indicating a much better crystallized structure. The more orderly and better crystalline structure can be explained by the lower electropolymerization rate of PANI polymers onto $WO_3$ coated ITO substrate,[12] which can be inferred from Figure 1. Peak shifts were also observed, and the 22.8 and 26.9° peaks shifted to 23.7 and 26.4°, respectively, indicating the crystalline structure change of the PANI matrix caused by the interactions between PANI and $WO_3$ nanoparticles, which are consistent with the results of FT-IR spectroscopy.

The HRTEM image in Figure 4 further confirmed the crystalline structure of the composite film. The lattice fringes observed in the image indicate that the film is crystallized. The lattice spacing of 0.228 nm corresponds to the *d*-spacing of the (113) plane of monoclinic $WO_3$ (PDF No. 00-043-1035). It

**Scheme 1. Possible Coordination Bonds Formed between PANI and WO$_3$ in PANI/WO$_3$ Nanocomposite Films**
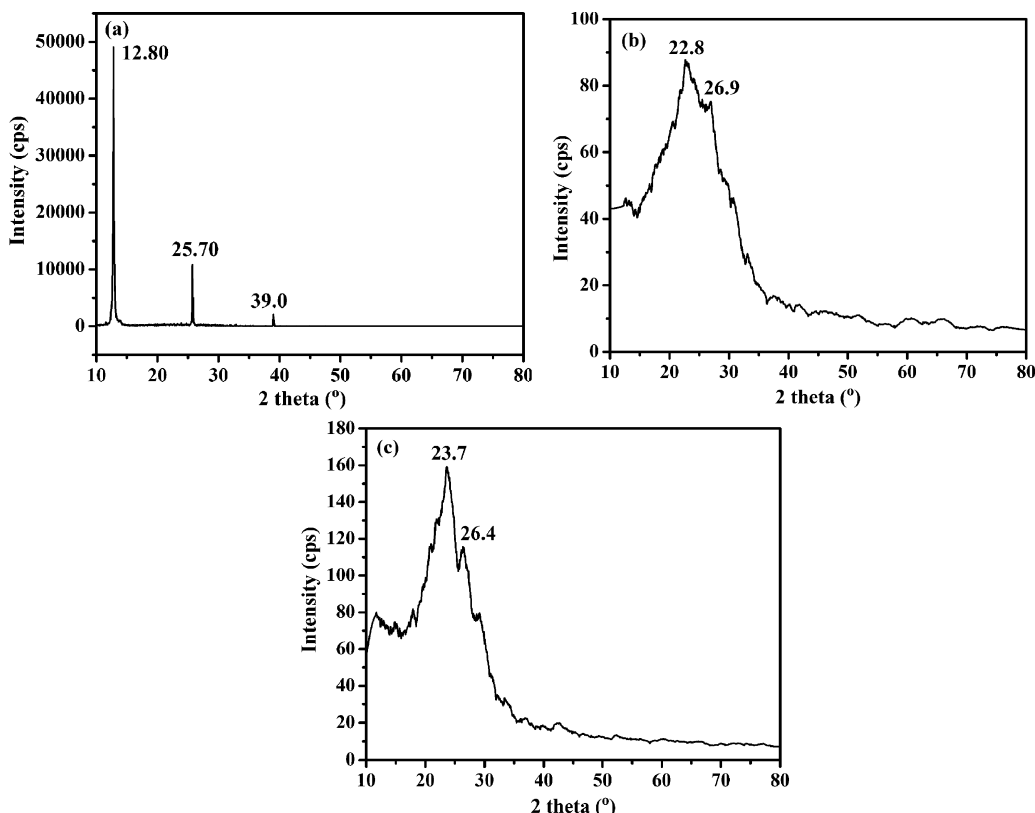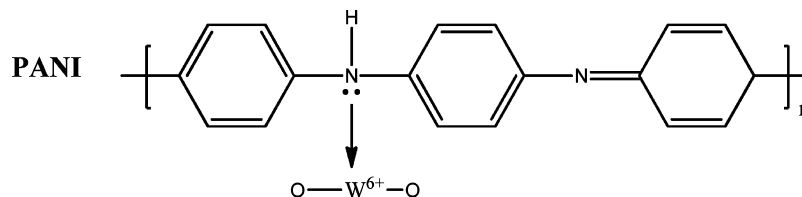




**Figure 3.** XRD patterns of (a) WO$_3$, (b) PANI, and (c) PANI/WO$_3$ composite films, respectively.
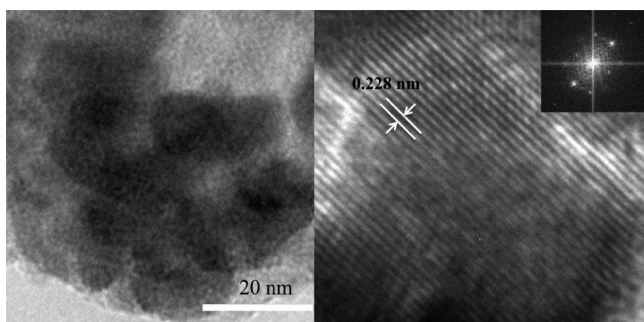


**Figure 4.** TEM image (left) and HRTEM image (right) of PANI/WO$_3$ composite film.

should be noted that XRD peaks of the WO$_3$ film could not be observed in the XRD test while the lattice fringes of WO$_3$ can be clearly seen in the HRTEM image. This phenomenon could be explained by different sample preparations. For the XRD test, the XRD patterns of the PANI/WO$_3$ composite film on the ITO glass substrate were measured. The diffraction peak of WO$_3$ cannot be observed because of the PANI film electropolymerized on the WO$_3$ film. For the TEM measurement, the composite film was scratched off from the substrate and suspended in ethanol

solution. The TEM samples were deposited from the suspension on a TEM grid after drying in air for TEM and HRTEM imaging, and thus well crystallized WO$_3$ was observed.

*3.2.3. AFM Results.* Figure 5 shows the AFM surface topography of the films on the left side, and the thickness of the films can be measured by large scans of section profiles on the right side. The composite film displays a morphology different from that of an individual WO$_3$ film or PANI film. The thicknesses of the WO$_3$ film, Figure 5a, and pure PANI film, Figure 5b, on ITO are measured to be 20 and 80 nm, respectively. For the nanocomposite film, Figure 5c, a thickness of 30 nm was measured. Therefore, less PANI was grown onto the WO$_3$ film compared to that grown on the bare ITO coated glass due to the increased substrate resistivity, which is in good agreement with the lower current peaks observed during the electropolymeriza-tion of aniline monomers (Figure 1).

**3.3. Electrochemical and Optical Properties.** *3.3.1. Cyclic Voltammetry.* The cyclic voltammograms of the films grown on the ITO coated glass slides were recorded in 0.5 M H$_2$SO$_4$ aqueous solution at a scan rate of 10 mV/s from −0.5 to 0.8 V. Parts a, b, and c of Figure 6 show the CV curves of the WO$_3$ film, PANI film, and PANI/WO$_3$ composite film, respectively. The WO$_3$ film, Figure 6a, displays an anodic peak A around 0.08 V,

**25055**

dx.doi.org/10.1021/jp3090777 | *J. Phys. Chem. C* 2012, 116, 25052−25064

**Figure 5.** AFM images (left) and section profiles (right) of (a) WO$_3$, (b) PANI, and (c) PANI/WO$_3$ composite films onto ITO glass, respectively.

which is associated with the deintercalation of H$^+$.[69] The well-defined profile of CV curve indicates a well crystallized structure,[70] which is in good agreement with XRD and TEM results. For the PANI film, two redox pairs, B/B′ and C/C′, originating from transitions from leucoemeraldine salt (LS) to emeraldine salt (ES) and emeraldine salt (ES) to pernigraniline salt (PS) of PANI, indicate the typical pesudocapacitance characteristic of the material.[71,72] The chemical structures of LS, ES, and PS of PANI are shown in Figure S1 in the Supporting Information. The corresponding intercalation/deintercalation of H$^+$ in the WO$_3$ film and oxidation/reduction transitions in the PANI film observed in the PANI/WO$_3$ composite film are illustrated as follows:

$$WO_3 + x(H^+ + e^-) \rightleftharpoons H_x W_{(1-x)}{}^{VI} W_x{}^{V} O_3$$
transparent $\qquad\qquad$ blue

$$LS \rightleftharpoons ES :$$

$$PANI + 2nHSO_4^- \rightleftharpoons (PANI)^{2n+}(HSO_4^-)_{2n} + 2ne^-$$
light yellow $\qquad\qquad$ green

$$ES \rightleftharpoons PS : \qquad PANI^{2n+}(HSO_4^-)_{2n} + 2nHSO_4^-$$
green

$$\rightleftharpoons (PANI)^{4n+}(HSO_4^-)_{4n} + 2ne^-$$
blue

A significant reduction of the oxidation potentials ($\sim$0.1 V) could also be observed for the composite film when compared to that of

**Figure 6.** CV curves of (a) WO$_3$ film, (b) PANI film, and (c) PANI/WO$_3$ composite film onto ITO, respectively, in 0.5 M H$_2$SO$_4$ at a scan rate of 10 mV/s.
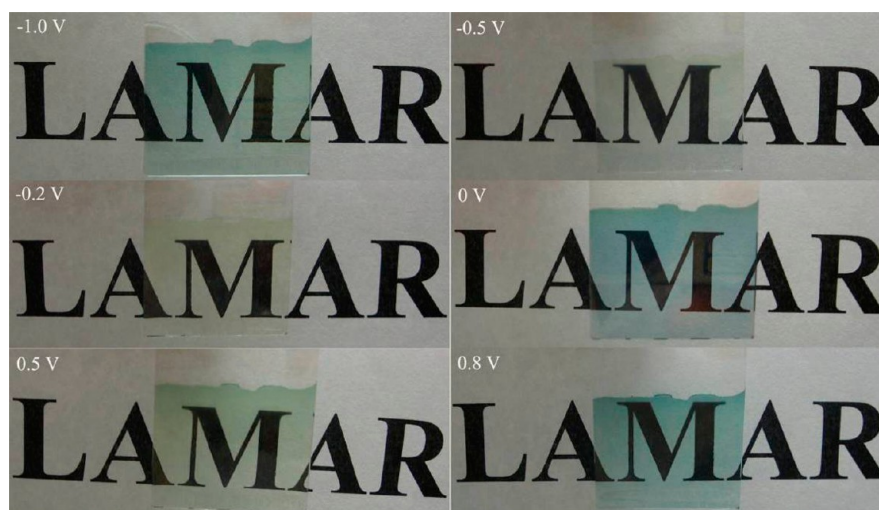


**Figure 7.** Color switching of the PANI/WO$_3$ composite film in 0.5 M H$_2$SO$_4$ at different potentials.

pure PANI, which might be due to the formation of a donor (PANI)−acceptor (WO$_3$) system.[52]

The composite film displayed multiple colors during the CV scanning, from blue at neutral potential to green at 0.5 V, and to blue at potentials more positive than 0.8 V. In the negative sweeping, the composite film first turned light yellow, and then light blue with the potential decreased to −0.5 V, and finally blue at −1.0 V. Figure 7 shows the color switching at different potentials.

*3.3.2. Spectroelectrochemistry of WO$_3$, PANI, and PANI/ WO$_3$ Composite Films.* Parts a, b, and c of Figure 8 show the UV−vis transmission spectra of WO$_3$ film, PANI film, and

PANI/WO$_3$ composite film at different potentials, respectively. For the WO$_3$ film, at a negative potential, i.e., −0.5 V, a significant absorbance in the wavelength ranging from 550 nm to a near-IR band caused by the H$^+$ intercalation can be observed.[52] As to the PANI film, a characteristic absorbance band distinguished around 750 nm is attributed to π−π* transition in the quinoid ring.[73] The PANI/WO$_3$ composite film exhibits UV−vis transmission spectra similar to PANI at positive potentials. At negative potentials, WO$_3$ plays an important role, and the spectrum begins to change (Figure 8d).

The coloration switching response of the films is also studied by applying potential steps of 0.8 and −0.2 V with a pulse width
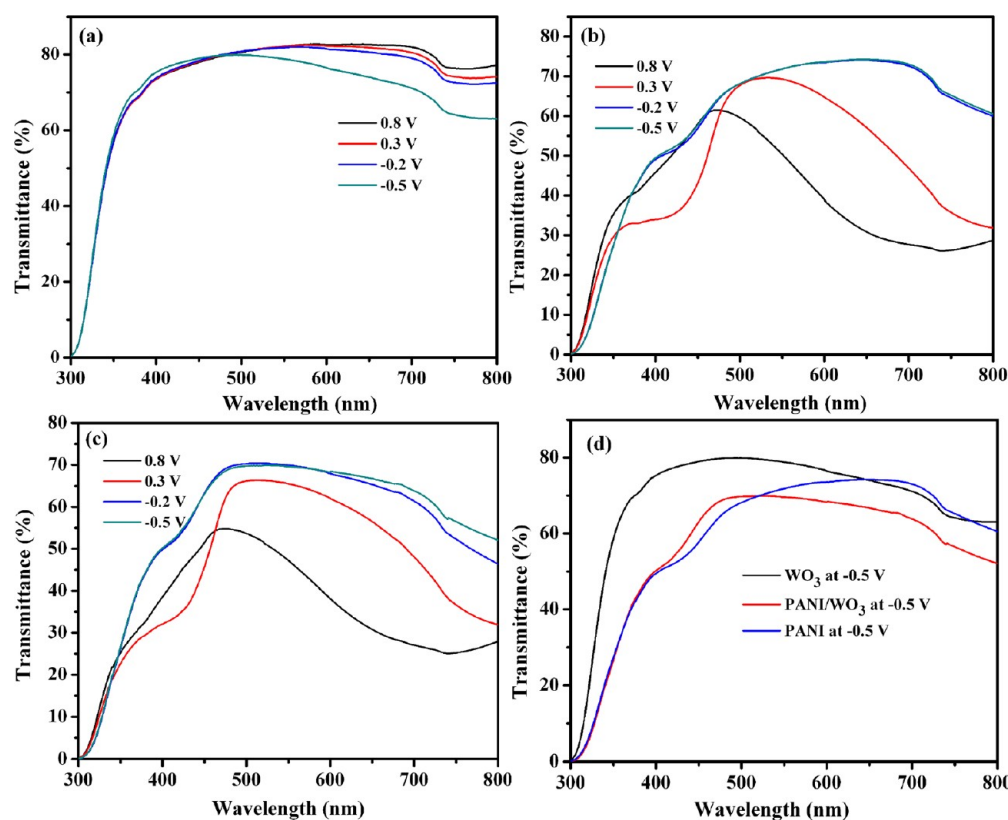
**Figure 8.** UV−vis spectra of (a) $WO_3$ film, (b) PANI film, and (c) PANI/$WO_3$ hybrid film on ITO in 0.5 M $H_2SO_4$ aqueous solution at different potentials. (d) UV−vis spectrum differences of these films at −0.5 V in 0.5 M $H_2SO_4$ aqueous solution.

of 20 s. The transmittance−time and corresponding charge density−time curves at 633 nm under an alternative square-wave voltage of 0.8 and −0.2 V are presented in Figure 9. A transmittance modulation of 5.4% (transmittance difference in the bleached and colored states in EC materials) for $WO_3$ is acquired, whereas much higher transmittance modulations of 37.4 and 35.3% are obtained for the PANI film and PANI/$WO_3$ hybrid film, respectively. The coloration time ($\tau_c$) and bleaching time ($\tau_b$) are defined as the times required for a 90% change in the full transmittance modulation, respectively.[74] The $WO_3$ film displays a response time longer than 20 s, since no plateau was reached within the time range. For PANI, $\tau_b$ is found to be 9.5 s and $\tau_c$ is 13.7 s from the first cycle in the transmittance−time curve, Figure 9 (left), and the composite film shows a slightly slower bleaching time of 9.9 s and nearly the same coloration time of 13.6 s. Therefore, it can be inferred that $WO_3$ substrate has almost no effect on the coloration kinetics of PANI.

The coloration efficiency (CE or $\eta$), which is defined as the change in optical density (OD) per unit charge ($Q$) inserted into (or extracted from) the EC films, i.e., the amount of energy to affect a color change, is an important consideration for the practical applications of EC materials in display and window devices. The CE can be calculated from eq 1:[75]

$$\eta = \Delta OD(\lambda)/Q_d \tag{1}$$

$$\Delta OD = \log[T_{bleached}/T_{colored}] \tag{2}$$

where $\Delta OD$ is the change in optical density, $\lambda$ is the dominant wavelength for the material, $Q_d$ is the charge density (injected/ejected charge per unit electrode area), $T_{bleached}$ refers to the transmittance of the film in the bleached state, and $T_{colored}$ refers to the varying transmittance of the film during the coloring

process. Figure 10 shows the plots of the calculated $\Delta OD$ obtained from the first cycle in the transmittance−time curve, Figure 9 (left), at a wavelength of 633 nm versus the corresponding inserted charge density obtained from the charge density−time curve, Figure 9 (right). The CE ($\eta$) is extracted as the slope of the line fitting to the linear region of the curve. Values of the CE are found to be 36.3, 50.0, and 98.4 cm$^2$ C$^{-1}$ for the $WO_3$ film, PANI film, and PANI/$WO_3$ hybrid film, respectively. The optical density for the $WO_3$ film does not change significantly, leading to a lower CE. Interestingly, a much higher CE is obtained for the composite film, indicating greater optical density change caused by fewer charges injected/ejected.

**3.4. Capacitive Performance for Energy Storage Applications.** *3.4.1. Electrochemical Impedance Spectroscopy (EIS).* EIS was employed to investigate the inner resistance of the films and their capacitance properties.[76] Parts a, b, and c of Figure 11 show Nyquist plots of the $WO_3$ film, PANI film, and PANI/$WO_3$ composite film onto ITO glass, respectively. The inner resistance, equivalent series resistance, which mainly arises from the electrolyte and the charge transfer in the film, is approximately 177, 22, and 196 Ω for the $WO_3$ film, PANI film, and PANI/$WO_3$ composite film, respectively, which is obtained from the intersection of the curve at the $X$-axis.[77] Therefore, it can be inferred that PANI imposes little resistance to the composite film, and $WO_3$ contributes primarily to the inner resistance. The Warburg resistance (diffusion impedance), that is, the 45° portion of the curve, results from the frequency dependent ion diffusion/transport in the electrolyte.[78] Both PANI film and PANI/$WO_3$ composite film exhibit a short 45° portion, indicating that PANI is an excellent material for the facilitation of ion transport to the inner electrolyte.[79]
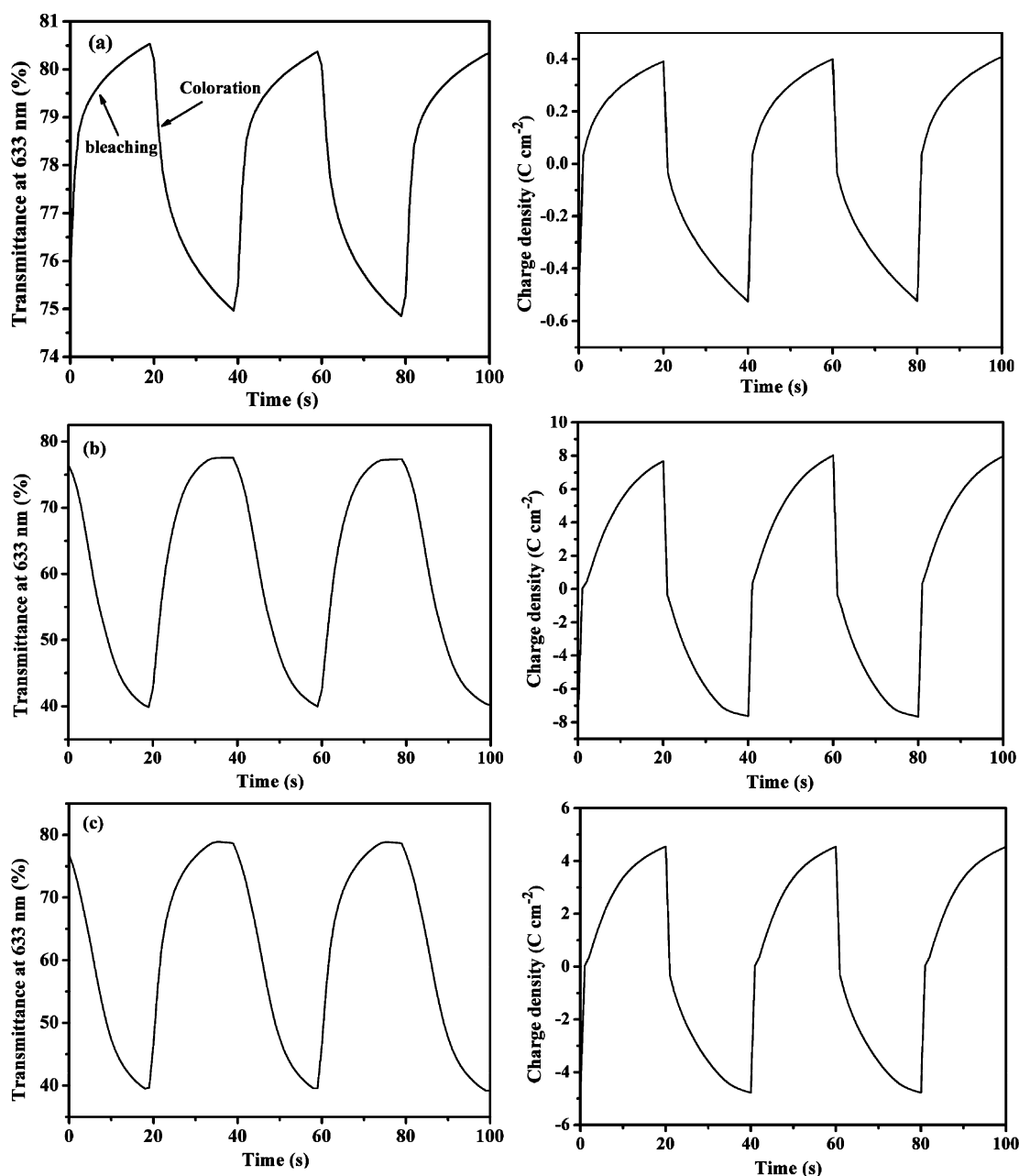
**Figure 9.** In situ corresponding transmittance (left) and chronocoulometry (right) of (a) WO$_3$ film, (b) PANI film, and (c) PANI/WO$_3$ hybrid film on ITO at 633 nm in 0.5 M H$_2$SO$_4$ aqueous solution. The tests were conducted under a square-wave voltage of 0.8 and −0.2 V with a pulse width of 20 s.

*3.4.2. Capacitance Evaluations of WO$_3$, PANI, and PANI/ WO$_3$ Composite Films.* Areal capacitance of the films was calculated from CV curves at different scan rates from −0.5 to 0.8 V in 0.5 M H$_2$SO$_4$ aqueous solution using eq 3:[79]

$$C_s = (2 \int i \, dV)/(S(\Delta V)\nu) \qquad (3)$$

where $C_s$ is the specific capacitance in F/cm$^2$, $\int i \, dV$ is the integrated area of the CV curve, $S$ is the surface area of active materials in the single electrode in cm$^2$, $\Delta V$ is the scanned potential window in V, and $\nu$ is the scan rate in V/s.

Parts a, b, and c of Figure 12 depict the CV curves and capacitance dependence on the scan rate of the WO$_3$ film, PANI film, and PANI/WO$_3$ composite film, respectively. At a low scan rate of 5 mV/s, the capacitance for the composite film is 0.025 F cm$^{-2}$, much higher than that for WO$_3$ (0.002 F cm$^{-2}$), and is of

the same order as that for PANI (0.075 F cm$^{-2}$). The capacitance is higher than what has been reported for pure PANI at a lower potential window of 1.0 V synthesized from a dilute polymerization process.[79] Even at a fast scan rate of 100 mV/s, the film could still deliver 0.009 F cm$^{-2}$, while the capacitances are 0.002 and 0.012 F cm$^{-2}$ for WO$_3$ film and PANI film, respectively. Therefore, it can be concluded that the composite film can retain most of the capacitance of PANI even at a broader potential window of 1.3 V. It should be noted that the areal capacitance of PANI film is higher than that of the composite film. This phenomenon can be explained by the fact of more aniline monomers electrodeposited onto bare ITO thus producing a thicker PANI film than the composite film,[80] as confirmed by CV synthesis and AFM results.

The galvanostatic charge−discharge measurements by chronopotentiometry (CP) were also carried out on the films in 0.5
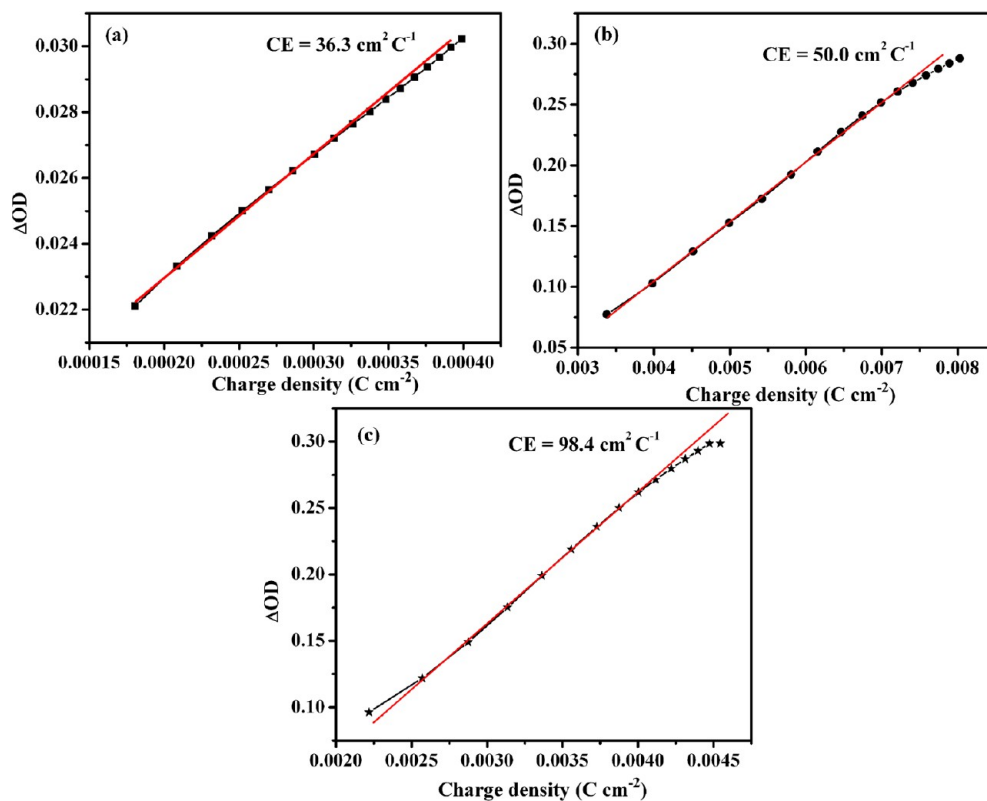
**Figure 10.** Plot of in situ optical density change ($\Delta OD$) versus charge density of (a) $WO_3$ film, (b) PANI film, and (c) PANI/$WO_3$ hybrid film. The optical density was measured at 633 nm at 0.8 V in 0.5 M $H_2SO_4$ aqueous solution.
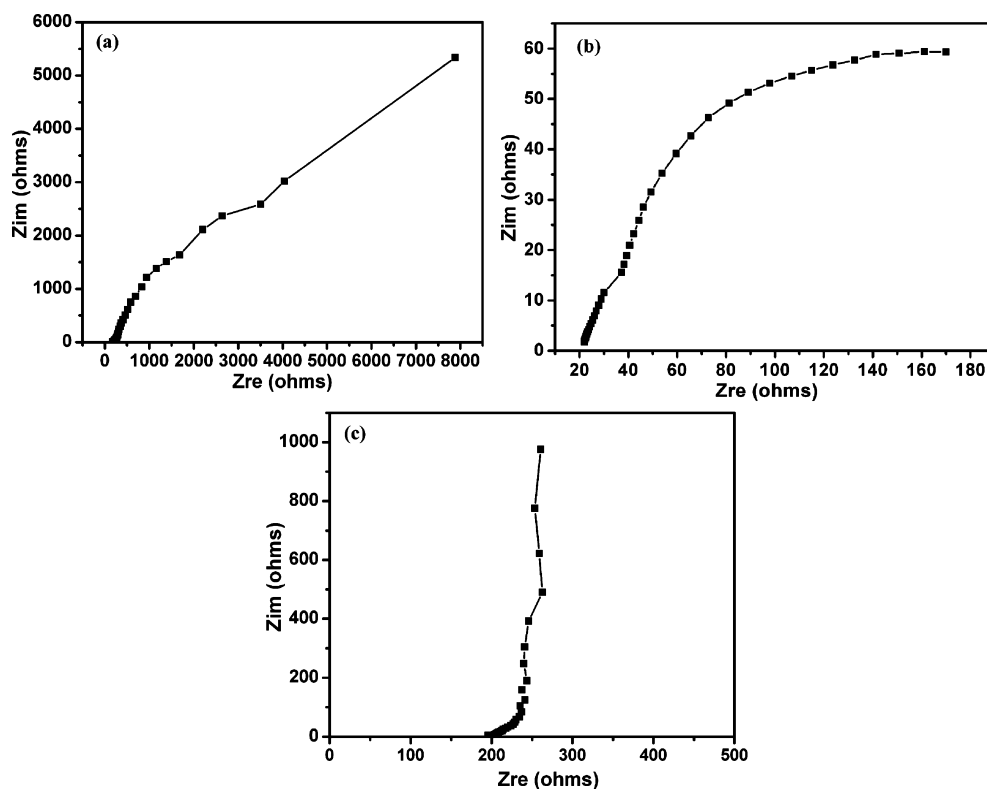


**Figure 11.** Electrochemical impedance spectroscopy (Nyquist plots) of (a) $WO_3$ film, (b) PANI film, and (c) PANI/$WO_3$ composite film, respectively, onto ITO in 0.5 M $H_2SO_4$ with a frequency loop from 100 kHz to 10 mHz using a perturbation amplitude of 5 mV at the open potential.

M $H_2SO_4$ aqueous solution to evaluate the areal capacitance of the films using eq 4:[79]

$$C_s = (2it)/(S\Delta V) \qquad (4)$$

25060

dx.doi.org/10.1021/jp3090777 | *J. Phys. Chem. C* 2012, 116, 25052−25064
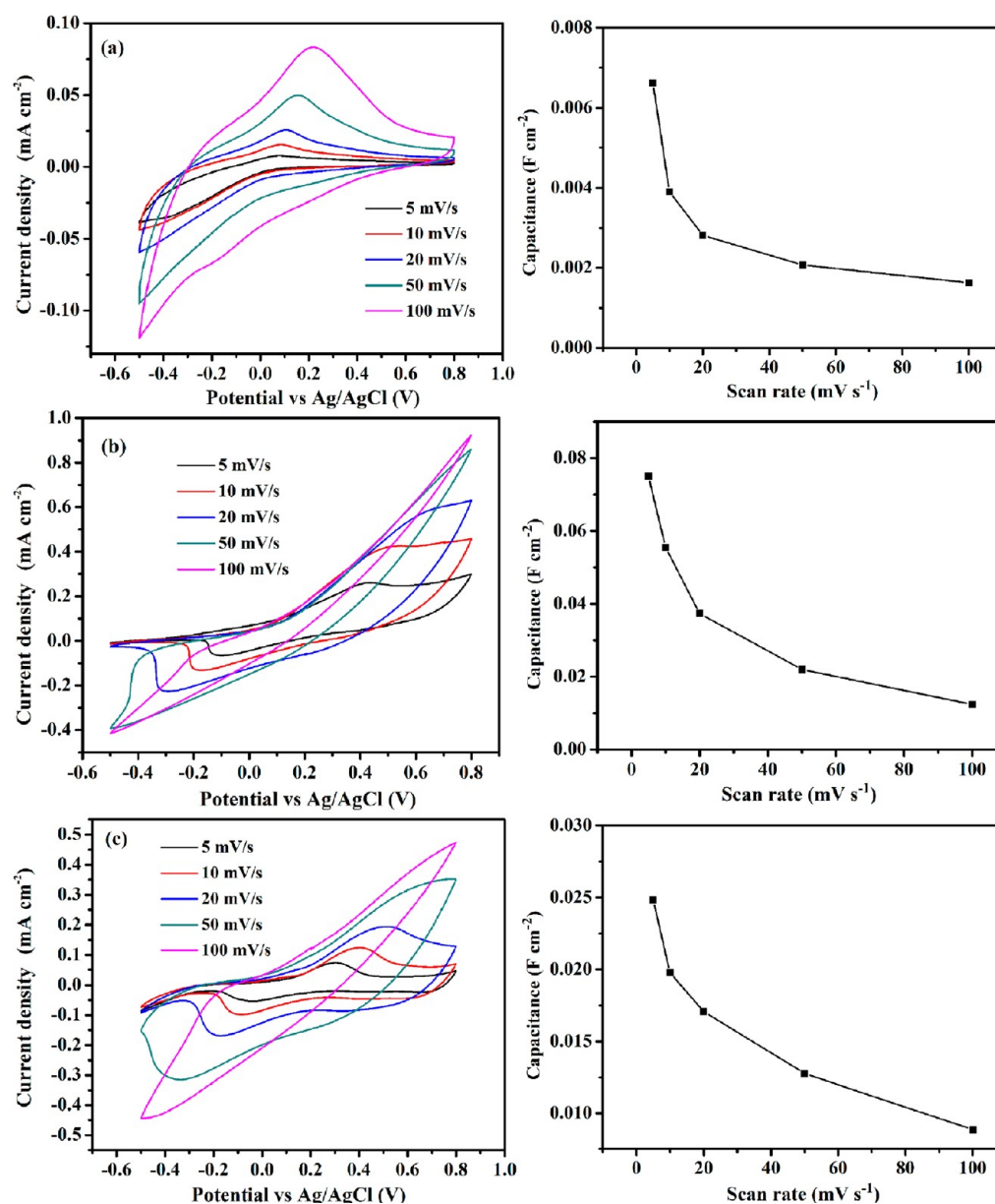
**Figure 12.** CV curves (left) and current density dependent areal capacitance (right) of (a) $WO_3$ film, (b) PANI film, and (c) PANI/ $WO_3$ hybrid films at different scan rates under a potential range from −0.5 to 0.8 V in 0.5 M $H_2SO_4$ aqueous solution.
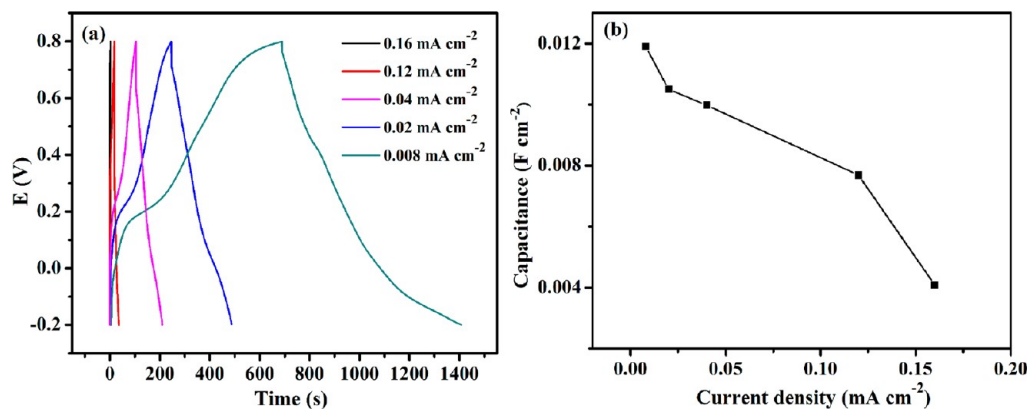


**Figure 13.** (a) Charge−discharge curves of PANI/$WO_3$ hybrid film at different current densities and (b) current density dependent areal capacitance of PANI/$WO_3$ in 0.5 M $H_2SO_4$ aqueous solution.

25061

dx.doi.org/10.1021/jp3090777 | *J. Phys. Chem. C* 2012, 116, 25052−25064
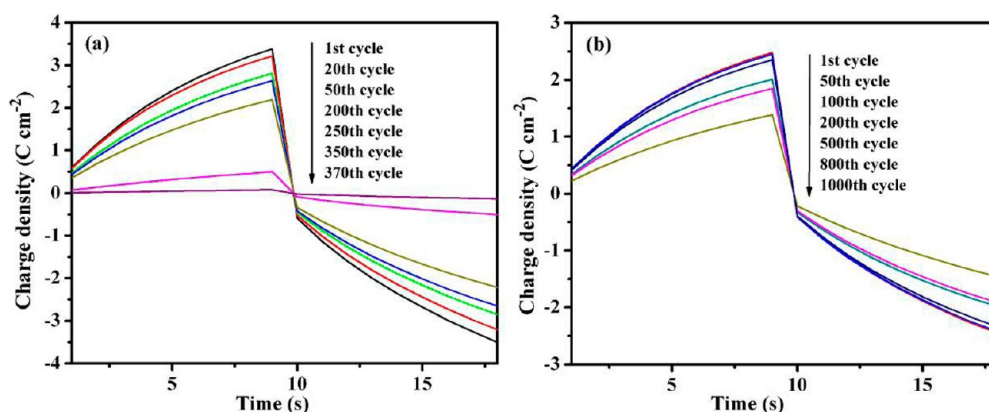
**Figure 14.** Charge−discharge cycles of (a) PANI film and (b) PANI/WO$_3$ hybrid film in 0.5 M H$_2$SO$_4$ aqueous solution. The potential step is 0.8 and −0.2 V holding for 10 s, respectively.

$C_s$ is the areal capacitance in F/cm$^2$, $i$ is the discharge current in A, $t$ is the discharge time in s, $S$ is the surface area of the active materials in the single electrode in cm$^2$, and $\Delta V$ is the scanned potential window (excluding IR drop in the beginning of the discharge) in V. Figure 13 shows the potential responses of the composite film under different currents and the dependence of areal capacitance of the composite film on current density. The areal capacitance of the composite film derived from the discharge in the charge−discharge curves is 0.012 F cm$^{-2}$ at a low current density of 0.008 mA cm$^{-2}$ and is 0.004 F cm$^{-2}$ at a high current density of 0.16 mA cm$^{-2}$. WO$_3$ is found to possess a small poor potential window at those current densities performed on the composite film, and it displays very quick discharge time at higher current density, for example, 6 mA cm$^{-2}$ (Figure S1 in the Supporting Information). For PANI, only capacitances at higher current densities can be obtained (Figure S1 in the Supporting Information). When the current density was lowered to 0.008 mA cm$^{-2}$, a significant degradation of PANI occurred and cracks were observed before the film was fully discharged (Figure S2 in the Supporting Information). These observed results are consistent with the reported poor electrochemical stability of PANI.[81]

**3.5. Stability of PANI/WO$_3$ Composite Film.** The stability of the composite film is also investigated using the charge−discharge method. Figure 14 depicts the charge density variation with time after different cycles. Compared to the PANI film, the PANI/WO$_3$ composite film exhibits much higher durability. The charge density did not change too much after 1000 cycles (Figure 14b). However, no energy storage function existed for PANI even after 370 cycles (Figure 14a). The chemical bonding formed between the polymer matrix and WO$_3$ particles, as justified by FT-IR results, Figure 2, is believed to play a vital role in enhancing the stability of the composite films.

## 4. CONCLUSIONS

The polyaniline/WO$_3$ nanocomposite films have been prepared by electrodeposition of PANI onto WO$_3$ coated ITO glass. The nanocomposite films display dual electrochromism and exhibit multiple colors at both positive and negative potentials. A coloration efficiency as high as 98.4 cm$^2$ C$^{-1}$ can be obtained. The composite films also possess areal capacitance comparable to that of the PANI films at a broad working potential window. The composite films demonstrate a much more enhanced durability than the PANI film during the charge−discharge cycles due to the chemical interaction between the polymer matrix and

the WO$_3$ particles. The polyaniline/WO$_3$ nanocomposite films show promising potentials for electrochromic and energy storage device applications.

## ■ ASSOCIATED CONTENT

**ⓢ Supporting Information**

Chemical structures of leucoemeraldine salt (LS), emeraldine salt (ES), and pernigraniline salt (PS) of PANI in H$_2$SO$_4$ aqueous solution, capacitances of the PANI film and WO$_3$ film at different current densities during the galvanostatic charge−discharge measurements in 0.5 M H$_2$SO$_4$ aqueous solution, and digital photograph of PANI film at a current density of 0.008 mA cm$^{-2}$ showing its poor electrochemical stability. This material is available free of charge via the Internet at http://pubs.acs.org.

## ■ AUTHOR INFORMATION

**Corresponding Author**

*E-mail: zhanhu.guo@lamar.edu (Z.G.); suying.wei@lamar.edu (S.W.). Tel.: (409) 880-7654 (Z.G.); (409) 880-7976 (S.W.). Fax: (409) 880-2197 (Z.G.); (409) 880-8270(S.W.).

**Notes**

The authors declare no competing financial interest.

## ■ REFERENCES

(1) Colvin, V.; Schlamp, M.; Alivisatos, A. *Nature* **1994**, *370*, 354−357.

(2) Holder, E.; Tessler, N.; Rogach, A. L. *J. Mater. Chem.* **2008**, *18*, 1064−1078.

(3) Descalzo, A. B.; Martínez-Máñez, R.; Sancenón, F.; Hoffmann, K.; Rurack, K. *Angew. Chem., Int. Ed.* **2006**, *45*, 5924−5948.

(4) Reiss, P.; Couderc, E.; De Girolamo, J.; Pron, A. *Nanoscale* **2011**, *3*, 446−489.

(5) Sudeep, P.; Emrick, T. *Polym. Rev.* **2007**, *47*, 155−163.

(6) De Girolamo, J.; Reiss, P.; Zagorska, M.; De Bettignies, R.; Bailly, S.; Mevellec, J. Y.; Lefrant, S.; Travers, J. P.; Pron, A. *Phys. Chem. Chem. Phys.* **2008**, *10*, 4027−4035.

(7) Aldakov, D.; Jiu, T.; Zagorska, M.; de Bettignies, R.; Jouneau, P. H.; Pron, A.; Chandezon, F. *Phys. Chem. Chem. Phys.* **2010**, *12*, 7497−7505.

(8) Zhu, J.; Wei, S.; Zhang, L.; Mao, Y.; Ryu, J.; Mavinakuli, P.; Karki, A. B.; Young, D. P.; Guo, Z. *J. Phys. Chem. C* **2010**, *114* (39), 16335−16342.

(9) Ding, K.; Jia, H.; Wei, S.; Guo, Z. *Ind. Eng. Chem. Res.* **2011**, *50* (11), 7077−7082.

(10) Wei, H.; Yan, X.; Li, Y.; Wu, S.; Wang, Y. A.; Wei, S.; Guo, Z. *J. Phys. Chem. C* **2012**, *116* (7), 4500−4510.

(11) Wei, H.; Yan, X.; Li, Y.; Gu, H.; Wu, S.; Ding, K.; Wei, S.; Guo, Z. *J. Phys. Chem. C* **2012**, *116* (30), 16286−16293.

(12) Li, Y.; Patil, R.; Wei, S.; Guo, Z. *J. Phys. Chem. C* **2011**, *115* (46), 22863−22869.

(13) Wang, C. C.; Song, J. F.; Bao, H. M.; Shen, Q. D.; Yang, C. Z. *Adv. Funct. Mater.* **2008**, *18*, 1299−1306.

(14) Zhu, J.; Wei, S.; Zhang, L.; Mao, Y.; Ryu, J.; Haldolaarachchige, N.; Young, D. P.; Guo, Z. *J. Mater. Chem.* **2011**, *21*, 3952−3959.

(15) Zotti, G.; Cattarin, S.; Comisso, N. *J. Electroanal. Chem. Interfacial Electrochem.* **1988**, *239*, 387−396.

(16) Liu, X. X.; Zhang, L.; Li, Y. B.; Bian, L. J.; Su, Z.; Zhang, L. J. *J. Mater. Sci.* **2005**, *40*, 4511−4515.

(17) Gu, H.; Tadakamalla, S.; Huang, Y.; Colorado, H. A.; Luo, Z.; Haldolaarachchige, N.; Young, D. P.; Wei, S.; Guo, Z. *ACS Appl. Mater. Interfaces* **2012**, *4* (10), 5613−5624.

(18) Zhu, J.; Gu, H.; Luo, Z.; Haldolaarachchige, N.; Young, D. P.; Wei, S.; Guo, Z. *Langmuir* **2012**, *28*, 10246−10255.

(19) Osaka, T.; Nakajima, T.; Naoi, K.; Owens, B. B. *J. Electrochem. Soc.* **1990**, *137* (7), 2139−2142.

(20) Bhadra, S.; Khastgir, D.; Singha, N. K.; Lee, J. H. *Prog. Polym. Sci.* **2009**, *34*, 783−810.

(21) Gospodinova, N.; Terlemezyan, L. *Prog. Polym. Sci.* **1998**, *23*, 1443−1484.

(22) He, S.; Hu, X.; Chen, S.; Hu, H.; Hanif, M.; Hou, H. *J. Mater. Chem.* **2012**, *22*, 5114−5120.

(23) Zhang, K.; Zhang, L. L.; Zhao, X.; Wu, J. *Chem. Mater.* **2010**, *22*, 1392−1401.

(24) Wang, D. W.; Li, F.; Zhao, J.; Ren, W.; Chen, Z. G.; Tan, J.; Wu, Z. S.; Gentle, I.; Lu, G. Q.; Cheng, H. M. *ACS Nano* **2009**, *3*, 1745−1752.

(25) Mishra, A. K.; Ramaprabhu, S. *J. Mater. Chem.* **2012**, *22*, 3708−3712.

(26) Zhu, J.; Chen, M.; Qu, H.; Zhang, X.; Wei, H.; Luo, Z.; Colorado, H. A.; Wei, S.; Guo, Z. *Polymer* **2012**, DOI: 10.1016/j.polymer.2012.10.002.

(27) Gu, H.; Rapole, S.; Sharma, J.; Huang, Y.; Cao, D.; Colorado, H. A.; Luo, Z.; Haldolaarachchige, N.; Young, D. P.; Wei, S.; Guo, Z. *RSC Adv.* **2012**, *2*, 11007−11018.

(28) Rajeshwar, K.; de Tacconi, N. R.; Chenthamarakshan, C. *Chem. Mater.* **2001**, *13*, 2765−2782.

(29) Coakley, K. M.; Liu, Y.; McGehee, M. D.; Frindell, K. L.; Stucky, G. D. *Adv. Funct. Mater.* **2003**, *13*, 301−306.

(30) Zhang, W.; Cheng, Y.; Yin, X.; Liu, B. *Macromol. Chem. Phys.* **2011**, *212*, 15−23.

(31) Beek, W. J. E.; Wienk, M. M.; Janssen, R. A. J. *Adv. Funct. Mater.* **2006**, *16*, 1112−1116.

(32) Kerr, T.; Wu, H.; Nazar, L. *Chem. Mater.* **1996**, *8*, 2005−2015.

(33) Janáky, C.; Visy, C.; Berkesi, O.; Tombácz, E. *J. Phys. Chem. C* **2009**, *113*, 1352−1358.

(34) Balaji, S.; Djaoued, Y.; Albert, A. S.; Brüning, R.; Beaudoin, N.; Robichaud, J. *J. Mater. Chem.* **2011**, *21*, 3940−3948.

(35) Lee, S. H.; Deshpande, R.; Parilla, P. A.; Jones, K. M.; To, B.; Mahan, A. H.; Dillon, A. C. *Adv. Mater.* **2006**, *18*, 763−766.

(36) Zhang, J.; Wang, X.; Xia, X.; Gu, C.; Zhao, Z.; Tu, J. *Electrochim. Acta* **2010**, *55*, 6953−6958.

(37) Wang, J.; Khoo, E.; Lee, P. S.; Ma, J. *J. Phys. Chem. C* **2008**, *112*, 14306−14312.

(38) Granqvist, C. *Sol. Energy Mater. Sol. Cells* **2000**, *60*, 201−262.

(39) Zhang, J.; Tu, J.; Xia, X.; Wang, X.; Gu, C. *J. Mater. Chem.* **2011**, *21*, 5492−5498.

(40) Wang, J.; Khoo, E.; Lee, P. S.; Ma, J. *J. Phys. Chem. C* **2009**, *113*, 9655−9658.

(41) Cheng, W.; Baudrin, E.; Dunn, B.; Zink, J. I. *J. Mater. Chem.* **2000**, *11*, 92−97.

(42) Wang, W.; Pang, Y.; Hodgson, S. N. B. *J. Mater. Chem.* **2010**, *20*, 8591−8599.

(43) Deepa, M.; Saxena, T.; Singh, D.; Sood, K.; Agnihotry, S. *Electrochim. Acta* **2006**, *51*, 1974−1989.

(44) Badilescu, S.; Ashrit, P. *Solid State Ionics* **2003**, *158*, 187−197.

(45) LeGore, L.; Lad, R.; Moulzolf, S.; Vetelino, J.; Frederick, B.; Kenik, E. *Thin Solid Films* **2002**, *406*, 79−86.

(46) Valyukh, I.; Green, S.; Arwin, H.; Niklasson, G.; Wäckelgård, E.; Granqvist, C. *Sol. Energy Mater. Sol. Cells* **2010**, *94*, 724−732.

(47) Livage, J.; Lemerle, J. *Annu. Rev. Mater. Sci.* **1982**, *12*, 103−122.

(48) Kepert, D. L.; Kyle, J. H. *J. Chem. Soc., Dalton Trans.* **1978**, 1781−1784.

(49) Claes, G. *Sol. Energy Mater. Sol. Cells* **2012**, *99*, 1−13.

(50) Ryu, K. S.; Moon, B. W.; Joo, J.; Chang, S. H. *Polymer* **2001**, *42*, 9355−9360.

(51) Gillaspie, D. T.; Tenent, R. C.; Dillon, A. C. *J. Mater. Chem.* **2010**, *20*, 9585−9592.

(52) Zhang, J.; Tu, J.; Zhang, D.; Qiao, Y.; Xia, X.; Wang, X.; Gu, C. *J. Mater. Chem.* **2011**, *21*, 17316−17324.

(53) Janáky, C.; De Tacconi, N. R.; Chanmanee, W.; Rajeshwar, K. *J. Phys. Chem. C* **2012**, *116* (6), 4234−4242.

(54) Takase, A.; Miyakawa, K. *Jpn. J. Appl. Phys.* **1991**, *30*, 1508−1511.

(55) Buron, C.; Lakard, B.; Monnin, A.; Moutarlier, V.; Lakard, S. *Synth. Met.* **2011**, 2162−2169.

(56) León-Silva, U.; Nicho, M.; Hu, H.; Cruz-Silva, R. *Sol. Energy Mater. Sol. Cells* **2007**, *91*, 1444−1448.

(57) Hong, S. Y.; Park, S. M. *J. Phys. Chem. B* **2005**, *109*, 9305−9310.

(58) Plesu, N.; Kellenberger, A.; Mihali, M.; Vaszilcsin, N. *J. Non-Cryst. Solids* **2010**, *356*, 1081−1088.

(59) Cui, S. Y.; Park, S. M. *Synth. Met.* **1999**, *105*, 91−98.

(60) Kellenberger, A.; Dmitrieva, E.; Dunsch, L. *J. Phys. Chem. B* **2012**, *116*, 4377−4385.

(61) El-Said, W. A.; Yea, C. H.; Choi, J. W.; Kwon, I. K. *Thin Solid Films* **2009**, *518*, 661−667.

(62) Zhu, J.; Wei, S.; Zhang, L.; Mao, Y.; Ryu, J.; Haldolaarachchige, N.; Young, D. P.; Guo, Z. *J. Mater. Chem.* **2011**, *21*, 3952−3959.

(63) Li, Y.; Zhao, X.; Xu, Q.; Zhang, Q.; Chen, D. *Langmuir* **2011**, *27* (10), 6458−6463.

(64) Gu, H.; Huang, Y.; Zhang, X.; Wang, Q.; Zhu, J.; Shao, L.; Haldolaarachchige, N.; Young, D. P.; Wei, S.; Guo, Z. *Polymer* **2011**, 801−809.

(65) Katoch, A.; Burkhart, M.; Hwang, T.; Kim, S. S. *Chem. Eng. J.* **2012**, *192*, 262−268.

(66) Stafström, S.; Bredas, J. L.; Epstein, A. J.; Woo, H. S.; Tanner, D. B.; Huang, W. S.; MacDiarmid, A. G. *Phys. Rev. Lett.* **1987**, *59*, 1464−1467.

(67) Wang, X.; Tang, S.; Liu, J.; He, Z.; An, L.; Zhang, C.; Hao, J.; Feng, W. *J. Nanopart. Res.* **2009**, *11*, 923−929.

(68) Zhang, X.; Zhu, J.; Haldolaarachchige, N.; Ryu, J.; Young, D. P.; Wei, S.; Guo, Z. *Polymer* **2012**, *53* (10), 2109−2120.

(69) Granqvist, C. *Electrochim. Acta* **1999**, *44*, 3005−3015.

(70) Avellaneda, C.; Bueno, P.; Faria, R.; Bulhoes, L. *Electrochim. Acta* **2001**, *46*, 1977−1981.

(71) Rudge, A.; Davey, J.; Raistrick, I.; Gottesfeld, S.; Ferraris, J. P. *J. Power Sources* **1994**, *47*, 89−107.

(72) Fusalba, F.; Gouérec, P.; Villers, D.; Bélanger, D. *J. Electrochem. Soc.* **2001**, *148*, A1−A6.

(73) Huang, W.; MacDiarmid, A. *Polymer* **1993**, *34*, 1833−1845.

(74) Argun, A. A.; Aubert, P. H.; Thompson, B. C.; Schwendeman, I.; Gaupp, C. L.; Hwang, J.; Pinto, N. J.; Tanner, D. B.; MacDiarmid, A. G.; Reynolds, J. R. *Chem. Mater.* **2004**, *16*, 4401−4412.

(75) Amb, C. M.; Dyer, A. L.; Reynolds, J. R. *Chem. Mater.* **2011**, *23*, 397−415.

(76) Barsoukov, E.; Macdonald, J. R. *Impedance Spectroscopy: Theory, Experiment, and Applications*; John Wiley and Sons: New York, 2005.

(77) Wang, Y.; Shi, Z.; Huang, Y.; Ma, Y.; Wang, C.; Chen, M.; Chen, Y. *J. Phys. Chem. C* **2009**, *113*, 13103−13107.

(78) Stoller, M. D.; Park, S.; Zhu, Y.; An, J.; Ruoff, R. S. *Nano Lett.* **2008**, *8*, 3498−3502.

(79) Wei, Z.; Wang, K.; Wu, H.; Meng, Y.; Zhang, Y. *Energy Environ. Sci.* **2012**, *5*, 8384−8389.

(80) Broughton, J. N.; Brett, M. J. *Electrochim. Acta* **2004**, *49*, 4439–4446.

(81) Mažeikienè, R.; Malinauskas, A. *Eur. Polym. J.* **2002**, *38*, 1947–1952.

**25064**

dx.doi.org/10.1021/jp3090777 | *J. Phys. Chem. C* 2012, 116, 25052–25064